JOURNAL OF GEOPHYSICAL RESEARCH, VOL. 104, NO. A12, PAGES 27,973–27,989, DECEMBER 1, 1999

Ionization by energetic protons in Thermosphere-Ionosphere Electrodynamics General Circulation Model

M. Galand[1] and R. G. Roble

High Altitude Observatory, National Center for Atmospheric Research, Boulder, Colorado

D. Lummerzheim

Geophysical Institute, University of Alaska, Fairbanks

Abstract. Originating in the magnetosphere and precipitating into the high-latitude ionosphere, energetic protons in the keV energy range are a common auroral phenomenon and can represent an important energy source for the auroral atmosphere. In global models describing the ionosphere-thermosphere interaction, keV protons have always been neglected or treated as if they were electrons. Here we investigate the effect of keV protons on both the ionospheric and thermospheric composition in the E region on a planetary scale. We present a parameterization of electron and ion production rates induced by an incident proton beam as a fast computational scheme for use in global models. The incident proton beam is assumed to have a Maxwellian distribution with characteristic energies between 1 and 20 keV. The parameterization is validated against a full proton transport code. By including these parameterized electron and ion production rates in a one dimension-in-space (1D-in-space) Thermosphere-Ionosphere Global Mean Model, we show that proton precipitation can cause a significant enhancement of the electron density, the major ion (O_2^+ and NO^+) densities, and the nitric oxide density. As a result, the conductivities in the E region are also greatly increased. Using the Thermosphere-Ionosphere Electrodynamics General Circulation Model (TIE-GCM), we show that the proton precipitation, when added to the normal electron aurora, causes a large increase (up to 70%) in electron, O_2^+, and NO^+ densities over much of the auroral oval. The NO density is affected in a larger area owing to the long lifetime of NO on the nightside. This first study of the influence of protons on a planetary scale clearly shows the significant impact that auroral keV protons can have on the ionospheric and thermospheric composition and the need to include proton precipitation in global models.

1. Introduction

Coming from the magnetosphere, electrons and protons in the keV energy range are a major energy source for the auroral upper atmosphere. This source often exceeds the local input from solar EUV and UV sources. The interaction of these particles with the atmosphere leads to electron and ion production, to heating, and to excitation inducing auroral photoemissions [e.g., *Rees*, 1987]. One of the results is that the electron density, which influences altimetry measurements or long-distance communications, is largely disturbed, as attested by incoherent scatter radar observations [e.g., *Anderson et al.*, 1997]. Another consequence of particle precipitation is the perturbation of the ionospheric and thermospheric temperatures; the increase of the neutral temperature leads to an expansion of the atmosphere, inducing orbital variations of satellites and affecting the location of space debris which may require position adjustments of the space shuttle. The aurora is also a source of nitric oxide (NO), which can spread over large portions of the globe owing to its long lifetime. Recent ultraviolet spectrometric observations from the Student Nitric Oxide Explorer (SNOE) satellite have shown that the NO density is strongly related to the auroral activity and particle precipitation [*Solomon et al.*, 1999, and references therein].

These impacts show that auroral particle precipitation plays a major role in affecting the high-latitude

[1]Now at Space Environment Center, NOAA, Boulder, Colorado.

Paper number 1999JA900374.
0148-0227/99/1999JA900374$09.00

atmosphere and thus space weather. The global models describing the thermosphere-ionosphere interaction must include the effects of auroral particle precipitation. To date, these global models, which are tools to understand and forecast the atmospheric state and behavior, encompass only electron precipitation [*Roble and Ridley*, 1987; *Roble*, 1992; *Codrescu et al.*, 1997] or assume all the keV particles to be electrons [*Fuller-Rowell and Evans*, 1987; *Fuller-Rowell et al.*, 1996]. The keV protons are neglected or treated as if they were electrons. However, satellite and ground-based measurements have shown that protons can represent an important, sometimes major, energy source in the ionosphere [*Hardy et al.*, 1989, 1991; *Newell et al.*, 1991]. Using a local auroral model based on a proton transport code, comparison of space- and ground-based observations has underlined the key role keV protons can play on the electron density in the auroral E region [*Senior et al.*, 1987; *Basu et al.*, 1987; *Lilensten and Galand*, 1998].

In the present paper we investigate, for the first time, the effect of keV auroral protons on both the thermosphere and the ionosphere on a planetary scale. The altitude region of interest is the E region between 100 and 160 km. The characteristic energy of the incident protons is taken in the $1 - 20$ keV energy range assuming a Maxwellian energy distribution. A comprehensive description of proton transport is achieved by solving the Boltzmann equation [*Galand et al.*, 1997]. In order to study the effect of protons on a planetary scale we include the results from the proton transport model in the National Center for Atmospheric Research (NCAR) Thermosphere-Ionosphere Electrodynamics General Circulation Model (TIE-GCM) [*Richmond et al.*, 1992]. This model requires very fast computational schemes. We develop simplified relations to estimate electron and ion production rates induced by an incident proton beam, as explained in section 2.

The validation of this parameterization is performed by comparison with our full proton transport. First we include the proton parameterization in the one dimension-in-space (1D-in-space) Thermosphere-Ionosphere Global Mean Model [*Roble*, 1995] (section 3). A comparison of the density profile of different atmospheric constituents is presented for the two cases, with and without proton precipitation. The effect on conductivities is also given. In addition, we discuss the case where protons are treated as if they were electrons. In section 4 a study on a planetary scale of the effect of protons is conducted using the TIE-GCM. The atmospheric response to proton precipitation is assessed for medium conditions of magnetic activity. Finally, section 5 summarizes our results and discusses the impact of protons on the thermosphere and the ionosphere in high-latitude regions.

2. Parameterization

An incident keV proton beam interacts with the ambient neutral species through different reactions, mainly ionization, excitation, and charge-changing reactions, namely, capture ($H^+ \rightarrow H$) and stripping ($H \rightarrow H^+$) [e.g., *Basu et al.*, 1993]. Ionization and capture lead to the production of ions; ionization and stripping lead to the production of electrons. The electron and ion production represents at least 95% of the total reaction rate and 95% of the total energy deposited in the atmosphere, mainly between 100 and 200 km. Therefore, to study the major direct effects induced by energetic protons in the E region of the atmosphere, the rates to parameterize are those associated with electron and ion production.

Parameterizations for the energy deposition rate for auroral electrons and protons have been derived by *Rees* [1963, 1982], *Reid* [1961], and *Jackman et al.* [1980]. A summary and comparison of these methods is found in the work of *Lummerzheim* [1992]. These parameterizations are based on range calculations. *Rees* [1982] has applied the parameterization to proton aurora, while Reid and Jackman et al. developed their energy deposition rates for high-energy protons that penetrate into the mesosphere. To obtain ionization rates from these methods, one has to assume a given relation between energy loss and ionization rate. We base our parameterization on a similar approach but provide functions for the individual ionization rates.

The simplified relations for the electron and ion production rates which are discussed in sections 2.1 and 2.2 are based on the semiempirical relation (1) given by *Rees* [1982] for the electron production rate (refer to (1) and (2) in the present paper). For the proton parameterization we derive the different parameters used, the range, the normalized energy deposition rate, and the energy loss per electron, from the transport code developed by *Galand* [1996]. This transport code solves the Boltzmann equation for protons and H atoms, using a new method which allows a multistream solution [*Galand et al.*, 1997]. This model has been validated by direct comparison with rocket data from the Proton I experiment [*Søraas et al.*, 1974] and by comparison with another code [*Basu et al.*, 1993].

The different quantities used in the parameterization of the electron and ion production rates are inferred from a set of runs of the transport code using an incident proton flux isotropic over the downward hemisphere and with a Maxwellian distribution in energy. The incident energy flux Q_0 is chosen as 1 erg cm^{-2} s^{-1}, providing normalized results. The characteristic energy E_0 of the incident beam is in the $1 - 20$ keV range, which is typical of auroral protons [*Hardy et al.*, 1989]. It should be pointed out that, for a Maxwellian distribu-

tion in energy, the characteristic energy E_0 is half of the mean energy $\langle E \rangle$ often used in studies dealing with particle flux measurements [*Hardy et al.*, 1989]. However, because we perform comparisons of different quantities with other theoretical studies, we keep the same convention as in those works and refer to the characteristic energy E_0.

The magnetic field is not included here as *Galand and Richmond* [1999] have shown that its effect is relatively insignificant on the electron production rate in the energy deposition region. Collisional angular redistribution is neglected, and no field-aligned electric field is considered. The calculations are assumed to be applied to the center of a wide incident beam, such that the lateral spreading can be neglected. The altitude grid extends from 800 km down to 90 km with 200 levels. The minimum energy of the energy grid is set to 100 eV, and the maximum energy depends on the chosen E_0: the number of levels for the energy grid is between 100 and 200. The cosine pitch angle grid is uniform with four levels. For all runs we adopted the neutral atmosphere model as given by Mass Spectrometer and Incoherent Scatter (MSIS) 90 [*Hedin*, 1991], for 70° latitude and 1900 local time in winter, with a magnetic activity index A_p of 20 and a solar index $F_{10.7}$ of 150, representative of average magnetic and solar conditions. The cross section set used is from *Basu et al.* [1987] and from *Rees* [1989]. The energy losses are those presented by *Galand et al.* [1997].

2.1. Electron Production Rate

As a good approximation, the electron production rate P_e in $\mathrm{cm^{-3}\ s^{-1}}$ can be assumed proportional to the energy deposition rate η:

$$P_e(z) = \frac{\eta(z)}{W_e}, \tag{1}$$

where z is the altitude in km, η is in eV $\mathrm{cm^{-3}\ s^{-1}}$ and W_e is the energy loss per electron, in eV per electron. The parameterization of the two quantities η and W_e is the topic of sections 2.1.1 and 2.1.2, respectively.

2.1.1. Energy deposition rate. The energy deposition rate η can be approximated by [*Rees*, 1982]

$$\eta(z) = \frac{Q_0}{1.602 \times 10^{-12} \times R} \times \rho(z) \times \lambda(r), \tag{2}$$

where Q_0 is the incident energy flux of the proton beam in erg $\mathrm{cm^{-2}\ s^{-1}}$, R is the range of protons in g $\mathrm{cm^{-2}}$, corresponding to the highest altitude above which all of the energy has been deposited, and ρ is the total mass density of the atmosphere in g $\mathrm{cm^{-3}}$. Function λ is the normalized energy deposition function which depends on the normalized scattering depth r, defined as

$$r = \frac{1}{R} \times \int_z^\infty \rho(z')\, dz'. \tag{3}$$

The function λ can be determined as follows:

$$\lambda(r) = \frac{\frac{dE}{dr}}{\int_0^1 \left(\frac{dE}{dr}\right) dr}, \tag{4}$$

where E is the energy of the precipitating protons or H atoms.

Assuming the proton beam in charge equilibrium below about 300 km [*Jasperse and Basu*, 1982], that is above the energy deposition region, the variation of energy in altitude is

$$\frac{dE}{dz} = -\sum_\alpha n_\alpha(z)\, L_\alpha(E), \tag{5}$$

where n_α is the density of the neutral species α (N_2, O_2, or O) in $\mathrm{cm^{-3}}$ and L_α is the energy loss for charge equilibrium in eV $\mathrm{cm^2}$. By definition, $L_\alpha(E) = \sum_{X=H^+,H} f_X(E)\, L_{\alpha,X}(E)$, with f_X, the fraction of the energetic particle X (proton or H atom) in charge equilibrium and $L_{\alpha,X}$, the total energy loss function of the energetic particle X to the neutral species α. $L_{\alpha,X}$ is a function of the cross section and energy loss of the different reactions between the neutral α and the particle X.

From (3) and (5) we deduce

$$\frac{dE}{dr} = -\frac{R}{\overline{M}}\, \overline{L}(E), \tag{6}$$

where $\overline{M}$ is the mean mass of the three neutral species in grams, and $\overline{L}$ is the mean energy loss defined as

$$\overline{L}(E) = \sum_\alpha c_{n_\alpha}\, L_\alpha(E), \tag{7}$$

with $c_{N_2} = 0.78$ and $c_{O_2} = c_O = 0.11$.

Integrating (6) over energy and over r (from 0 to 1), the range R can then be defined as

$$R = \overline{M} \int_{E_{\min}}^{2\,E_0} \frac{dE}{\overline{L}(E)}, \tag{8}$$

where E_0 is the characteristic energy of the incident proton beam and $E_{\min}$ is the minimum energy below which the energy flux is negligible.

The loss function $\overline{L}$ can be approximated by a power law:

$$\overline{L}(E) = K_L\, E^{K_E}, \tag{9}$$

with the energy E in eV. Equation (8) becomes

$$R = \frac{\overline{M}}{K_L\,(1-K_E)} \left[(2\,E_0)^{(1-K_E)} - E_{\min}^{(1-K_E)}\right]. \tag{10}$$

Table 1. Parameters K_E and K_L Used in Equation (9) for Different Ranges of E_0

	E_0, keV					
	1.0 – 1.5	1.5 – 2.5	2.5 – 3.5	3.5 – 6.5	6.5 – 13.5	13.5 – 20.0
K_E	0.92	0.92	0.90	0.883	0.84	0.87
K_L	8.0×10^{-18}	7.0×10^{-18}	7.0×10^{-18}	7.0×10^{-18}	8.1×10^{-18}	4.5×10^{-18}

For E_0, $1 \leq E_0 \leq 20$ keV.

This is inserted into (4) and (6), and from integration we get

$$\lambda(r) = \frac{K_L \times R}{\overline{M}\,(2\,E_0 - E_{\min})} \left[(1-K_E)\,\frac{K_L \times R}{\overline{M}}\,(F_E - r)\right]^{\frac{K_E}{1-K_E}}, \quad (11)$$

with $F_E = \left[(2\,E_0)^{(1-K_E)} \times \overline{M}\right] / \left[(1-K_E)\,K_L \times R\right]$.

In (10) and (11) the energies E_0 and $E_{\min}$ are in eV. The derivation of (11) requires $(1-K_E)(F_E - r) > 0$. Our parameterization insures that $(1-K_E)$ is always positive (see Table 1), and F_E is smaller than r only at altitudes much below the energy deposition region. Therefore we set the normalized function $\lambda(r)$ to 0 where $F_E - r \leq 0$.

The coefficients K_L and K_E in (9) are found from a set of runs of the full transport model as discussed in the introduction of section 2. The values for K_L and K_E for different characteristic energies are given in Table 1. For a characteristic energy E_0 of 5 keV the energy loss function defined by (7) and that parameterized by (9) are presented in Figure 1a. The normalized energy deposition function λ can be determined easily from (10) and (11). The approximated λ obtained by taking a minimum energy $E_{\min}$ of 100 eV is shown in Figure 1b. This approximated λ is very similar to the normalized energy deposition function given by *Basu et al.* [1987], which was directly deduced from their transport code. This good agreement validates the approximation applied on the energy loss function by the power law in (9).

The energy deposition rate can now be computed from (2) using (10) and (11) and the coefficients in Table 1. The altitude profile of the approximated η is shown as a dashed line in Figure 1c. The energy deposition rate deduced from the proton and H atom fluxes as calculated by the transport code is defined as follows:

$$\eta(z) = 2\,\pi \sum_{\alpha} n_\alpha(z) \sum_{X=H^+,H} \sum_{k} \int\int dE\; d\mu\; \sigma^k_{\alpha,X}(E)\; W^k_{\alpha,X}(E)\; \Phi_X(z,E,\mu). \quad (12)$$

It is shown as a solid line in Figure 1c. Quantities $\sigma^k_{\alpha,X}$ and $W^k_{\alpha,X}$ are the cross section in cm^2 and the energy loss in eV, respectively, associated with the collision process k (ionization, excitation, or charge-changing reaction) occurring between the neutral of species α and the energetic particle X. Quantity Φ_X, the particle flux in cm^{-2} s^{-1} eV^{-1} sr^{-1}, as a function of altitude z, energy E, and cosine pitch angle μ, is the direct output of the transport code. The agreement between the approximated rate and that taken as reference is very good. The value of the peak from the parameterization is 6% higher compared to the reference. It has to be noted that the choice of another value for $E_{\min}$, a value lower than 100 eV, affects both r and λ but does not significantly affect the energy deposition rate.

2.1.2. Energy loss per electron. The energy loss per electron, W_e, represents the energy loss by an energetic particle between two successive productions of an electron. Assuming that it is independent of the altitude, an average value for W_e can be defined as the total energy lost in the atmosphere by the proton beam divided by the total number of electrons produced, that is,

$$W_e = \frac{\int \eta(z)\,dz}{\int P_e(z)\,dz}. \quad (13)$$

The incident beam is assumed to be composed only of protons. As the proton beam penetrates the atmosphere, it moves toward charge equilibrium by increasing the H atom fraction in the beam. The capture producing an H atom occurs then more often than the stripping producing a proton. The former leads to the production of an ion while the latter produces an electron. Therefore, as long as the beam is not at charge equilibrium, the electron and ion production rates are different. However, the energy deposition region where most of the ions and electrons are produced is located lower, in a region where the beam has reached charge equilibrium. The difference of the total number of captures compared with that of stripping cannot exceed the number of incident protons, which is very small compared with the number of electrons and ions produced. As a consequence, the integrated electron and ion production rates are almost equal, and it is suitable to call W_e, the "energy loss per electron-ion pair", a phrase used by *Basu et al.* [1993] or by *Kozelov and Ivanov* [1994]. For our parameterization we prefer to keep here the strict denomination of "energy loss per electron" in order to avoid confusion with the energy losses per ion associated with a given neutral species and a given en-

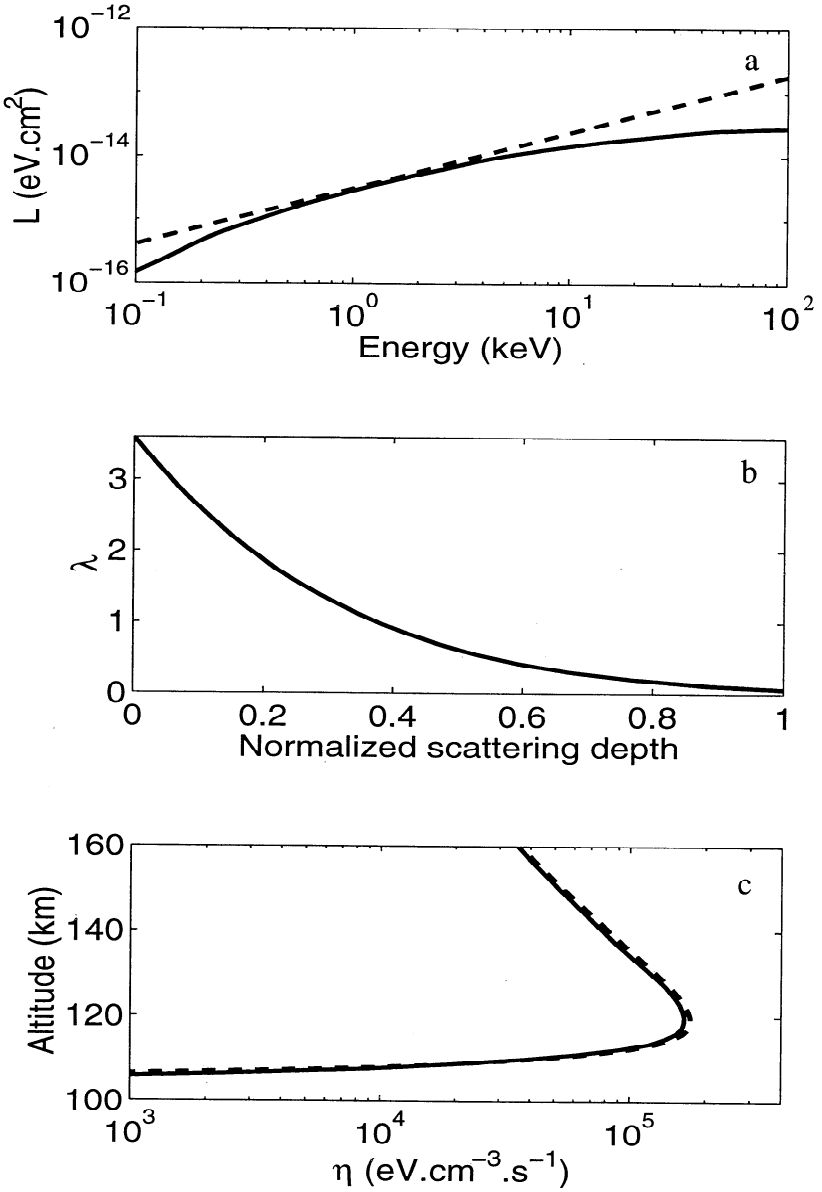

Figure 1. Results for a characteristic energy E_0 of 5 keV. (a) Total energy loss function at charge equilibrium as a function of the energy of the proton or H atom. The function deduced from (7) is plotted as a solid line; the parameterized one defined by (9) is plotted as a dashed line. (b) Normalized energy deposition function as a function of the normalized scattering depth, obtained from the parameterized energy loss function. (c) Altitude profiles of the energy deposition rate, obtained from the transport code (solid line) and deduced from the parameterization (dashed line). The incident energy flux Q_0 is equal to 1 erg cm^{-2} s^{-1}.

ergetic particle, quantities which will be introduced in section 2.2.

Using the set of runs discussed in the introduction of section 2, we have parameterized the energy loss per electron as a function of the characteristic energy E_0 of the incident beam. The result of this parameterization, given in Table 2, is presented as a thick solid line in Figure 2. *Kozelov and Ivanov* [1994] argue that at low energies, collisional angular redistribution could induce an increase of the energy loss per electron. For a monoenergetic beam of 2 keV they found an enhancement of 10% of W_e. However, using our transport code with the same input parameters for collisional angular redistribution as those described by *Galand et al.* [1998], we found no significant change of W_e. Owing to the lack of or the poor information about the phase functions and the elastic scattering cross sections, one cannot come to a definitive answer about the possible influence of the collisional angular redistribution on W_e. Assuming the effect to be small, we neglect collisional angular redistribution in the present study.

Our parameterization does not take into account the

Table 2. Energy Loss per Electron or Ion Parameterized as $W_{\alpha,X}(E_0) = \sum_l a_l \; E_0^l$

	Electron	(N_2, H^+)	(N_2, H)	(O_2, H^+)	(O_2, H)	(O, H^+ or H)
a_0	18.94	37.90	156.68	8.01×10^{-1}	14.26	28.81
a_1	1.32	2.95×10^{-1}	−63.86	2.09	2.73	32.69
a_2	-8.25×10^{-2}	2.03×10^{-1}	17.33	-2.91×10^{-2}	-8.55×10^{-2}	−1.83
a_3	3.80×10^{-3}	-1.57×10^{-2}	−2.32	1.58×10^{-4}	2.93×10^{-3}	4.02×10^{-2}
a_4	-7.06×10^{-5}	3.44×10^{-4}	1.64×10^{-1}	0	0	0
a_5	0	0	-5.83×10^{-3}	0	0	0
a_6	0	0	8.21×10^{-5}	0	0	0

$W_{\alpha,X}$ is given in eV per electron (or per ion), and E_0 is given in keV ($1 \leq E_0 \leq 20$ keV).

secondary electron production. This additional ionization is produced by the proto-electrons; we use this phrase to identify electrons directly produced by interaction between the proton beam and the atmosphere. The proto-electrons can be energetic enough to ionize the ambient neutral species. Using a coupled electron-proton transport code, *Lilensten and Galand* [1998] estimated this secondary electron production as $P_{e2} = 0.006 \times E_0 \times P_e$, where E_0 is in the $1 - 50$ keV range and P_e in $cm^{-3}\ s^{-1}$ represents the primary electron production, that is, the production of proto-electrons given by (1). When this secondary ionization is taken into account, W_e decreases to the lower border of the shaded area drawn in Figure 2. At an E_0 of 20 keV the decrease is up to 12%, and at a more typical E_0 of 10 keV it is 6%. This change is small enough that we can neglect the secondary electron ionization in the present study dedicated to infer approximative relations.

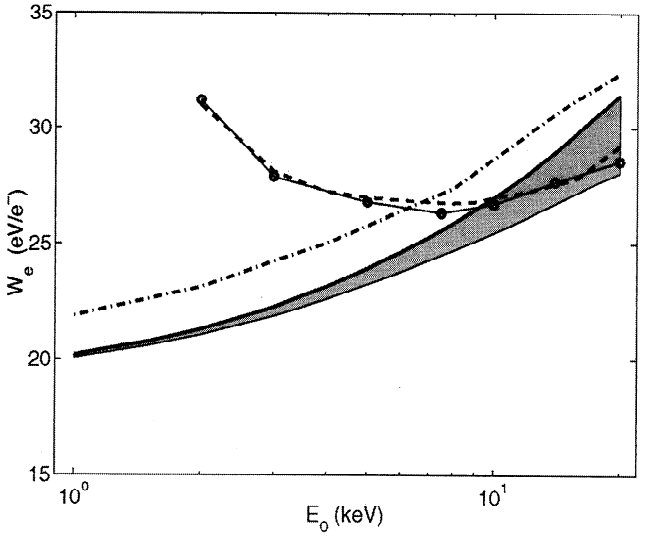

Figure 2. Energy loss per electron as a function of the characteristic energy of the incident proton beam. The thick solid line from our transport code ($E_{\min}$ = 0.1 keV and W_e deduced from η) is used in the parameterization. When the secondary electron production is included, W_e decreases down to the lower border of the shaded area. The dashed line is from *Strickland et al.* [1993], and the solid line with circles is from our transport code with the same assumptions as those used by Strickland et al. ($E_{\min}$ = 1 keV, W_e deduced from Q_0, and secondary electron production rate added). The dash-dotted line is from *Decker et al.* [1996].

Also shown as a dashed line in Figure 2 is the energy loss W_e obtained by *Strickland et al.* [1993] and *Basu et al.* [1993]. At low energies there is a large discrepancy between this curve and our parameterized results. This difference arises from the definition of total energy available (the denominator in (13)) and the low-energy cutoff that the two models use. Strickland et al. start the energy grid at 1 keV, while our model extends to 0.1 keV. Rather than using the total energy deposited in the atmosphere, they use the total energy influx at the top of the atmosphere in the denominator of (13). For a better comparison we also used an $E_{\min}$ of 1 keV, included the secondary ionization from the proto-electrons, as Strickland et al. did, and made the definition of the total energy deposited consistent. The results obtained under these conditions (thin line with circles in Figure 2) are in very good agreement with the results by Strickland et al.. Note that the difference between the mean energy from the computation with $E_{\min}$ = 1 keV and $E_{\min}$ = 0.1 keV becomes negligible for high characteristic energies but is important for low-energy proton precipitation. For low characteristic energies, the ionization by precipitating particles below the energy grid cutoff becomes important, contributing to the difference.

More recently, *Decker et al.* [1996] applied the proton transport code of *Basu et al.* [1993] as well as the Monte Carlo code of *Kozelov* [1993] to find the energy loss per electron, which is shown as the dash-dotted line in Figure 2. These results were obtained by neglecting the magnetic field, the collisional angular redistribution, and the secondary electron production. The curve found by *Decker et al.* [1996] has a very similar shape compared with that representative of our parameterized results. The displacement is less than 8% everywhere and 3% at the high energy end, and it can be attributed to small differences in the model parameters (minimum energy and cross sections).

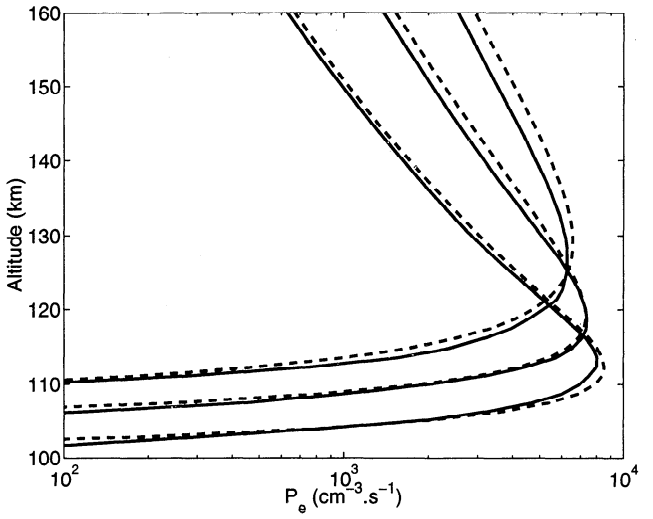

Figure 3. Altitude profiles of the electron production for a characteristic energy E_0 of 1, 5, and 15 keV from top to bottom. The solid lines are from the transport code, and the dashed lines are from the parameterization. The incident energy flux Q_0 is equal to 1 erg cm^{-2} s^{-1}.

2.1.3. Validation. Using the energy deposition rate given by (2) and computing the energy loss per electron from Table 2, the electron production rate P_e is determined from (1). The altitude profile of the electron production rate from the parameterization is shown by the dashed lines in Figure 3 for different characteristic energies E_0. The solid lines are the electron production rates deduced directly from the proton transport code and taken as reference:

$$P_e(z) = 2\pi \sum_{\alpha} n_\alpha(z) \sum_{X=H^+,H} \int\int dE\ d\mu\ \sigma^{\mathrm{ioni}}_{\alpha,X}(E)\ \Phi_X(z,E,\mu) + 2\pi \sum_{\alpha} n_\alpha(z) \int\int dE\ d\mu\ \sigma^{01}_{\alpha}(E)\ \Phi_H(z,E,\mu). \quad (14)$$

The superscript "ioni" stands for ionization, and "01" stands for stripping. There is a very good agreement between the approximated profiles and the reference profiles. Note that with increasing E_0 the maximum of the electron production rate decreases in altitude. Over the whole range of E_0 (1 – 20 keV) the error of the altitude of the peak is ±1 km (except below 2 keV with 3 km), and the error in magnitude is less than 10%. To this parameterization error, we must add uncertainties coming from the numerical calculations (less than 3%), the uncertainties in the cross sections (up to 30%), the uncertainties of the neutral atmosphere model and of the incident flux (distribution in energy and angle), and the error induced by neglecting collisional angular redistribution (for low E_0) and secondary electron ionization (for high E_0). All together, the uncertainty in the electron production rate around the peak is dominated by the input parameters rather than by the approximations in the parameterization.

2.2. Ion Production Rates

The determination of the ion production rates is done in two steps. First the ionization rates are computed for every neutral species. Second we apply fragmentation ratios to obtain the ratio of dissociative ionization. The fragmentation ratios and the ionization rates depend on the type of energetic particle (proton or H atom) that causes the ionization.

The first stage is the parameterization of the ionization rates. We specify individual ionization rates for a given neutral species α and a given energetic particle X (proton or H atom). Even though the term "ionization" is used, it implies the production of ions from both ionization and capture. By analogy with the electron production given by (1), the ionization rate in cm^{-3} s^{-1} is assumed to be given by

$$P_{\alpha,X} = \mathcal{S}_\alpha(z) \times \frac{\eta(z)}{W_{\alpha,X}}, \quad (15)$$

where $\mathcal{S}_\alpha$ is a shape factor introduced to account for the difference of shape between η and $P_{\alpha,X}$, η in eV cm^{-3} s^{-1} is defined by (2), and $W_{\alpha,X}$ in eV per ion is the energy loss per ion produced by interaction of a neutral α with a particle X. The parameteriza-

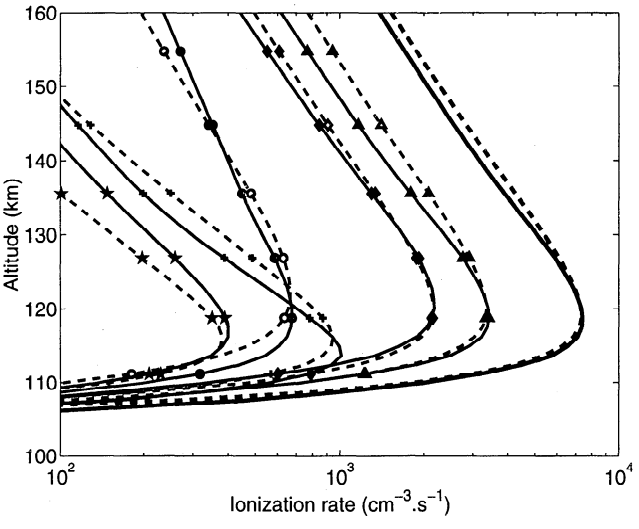

Figure 4. Altitude profiles of the ionization rate for a characteristic energy E_0 of 5 keV and an incident energy flux Q_0 of 1 erg cm^{-2} s^{-1}. The triangles correspond to (N_2, H^+), the diamonds correspond to (N_2, H), the crosses correspond to (O_2, H^+), the stars correspond to (O_2, H), and the circles correspond to (O, H^+ or H). The lines without symbols represent the total of all contributions, the electron production rate. The solid lines are from the transport code, and the dashed lines are from the parameterization.

tion for the shape factors and the energy losses per ion is deduced from the set of runs described in the introduction of section 2. As illustrated in Figure 4, the total ion production in the lower thermosphere is mainly influenced by the ionization rates associated with the major neutral, that is N_2. Therefore the altitude profile of $P_{N_2,X}$ is relatively close to that of P_e and η: $\mathcal{S}_{N_2}$ equals 1. However, the shape of the oxygen ionization rates differs from P_e and η. This is mainly related to the altitude variation of the proportion of the different neutral species. The different cross sections induce a minor contribution to the shape factor. Because the proportion of O decreases in density with decreasing altitudes and the proportion of O_2 increases, the direct O ionization peaks higher than that of O_2. The shape factors are constructed as functions of the neutral densities:

$$\mathcal{S}_{O_2} = \frac{0.1\ n_{O_2}}{0.1\ n_{O_2} + n_O} \qquad \mathcal{S}_O = \frac{n_O}{0.7\ n_{O_2} + n_O}.$$

$W_{\alpha,X}$ is introduced by analogy with W_e. Because the shape of $P_{\alpha,X}$ can be relatively different from η and because the region of the peak must be approximated best, $W_{\alpha,X}$ is defined as follows:

$$W_{\alpha,X} = \frac{\max_z(\mathcal{S}_\alpha(z) \times \eta(z))}{\max_z(P_{\alpha,X}(z))}, \tag{16}$$

where η and $P_{\alpha,X}$ are those deduced from the transport code from (12) and (14), respectively. Note that to compute $P_{\alpha,X}$, an equation similar to (14) must be used without applying the sums over α and X but taking all appropriate terms individually. Using our set of standard transport runs (section 2), the energy losses per ion have been parameterized as shown in Table 2.

Finally, the ionization rates are normalized such that at each altitude level, $\sum_{\alpha,X} P_{\alpha,X} = P_e$. As mentioned in section 2.1.2, at high altitudes where the proton beam is not yet at charge equilibrium, electron production rates and total ionization rates are different. However, in the region of interest, where the peak of the energy deposition is located, the electron and total ionization rates are equal, and it is a suitable assumption to apply this normalization.

The ionization rates computed directly from the transport code and from the parameterization of (15) are compared in Figure 4 with solid and dashed lines, respectively. These profiles have been obtained with an incident flux of 5 keV for E_0. The reference and the approximated curves are in good agreement. The error of the peak value is less than 7%, and the error of the peak altitude is less than 4 km. Over the whole range of E_0, the error in magnitude is less than 20%, and the error on the peak altitude is less than ±4 km (except below E_0 of 3 keV for which the variation can be up to 7 km). In the peak region the contribution of the different neutral species depends on local neutral densities and on the ratio of cross sections between different reactions, which results in a dependence on characteristic energy. For energies higher than 3 keV the ionization rates are dominated by the major neutral, N_2. At lower E_0, because the capture cross sections gain importance, $P_{\alpha,H+}$ are larger than $P_{\alpha,H}$.

The second step of the computation of the ion production rates is the application of fragmentation ratios $\mathcal{F}_{\alpha,X}$ to the ionization rates of the molecular species N_2 and O_2. These fragmentation ratios $\mathcal{F}_{\alpha,X}$ are defined as

$$\mathcal{F}_{N_2,X} = \frac{\sigma_{N^+,X}}{\sigma_{N_2^+,X}} \qquad \mathcal{F}_{O_2,X} = \frac{\sigma_{O^+,X}}{\sigma_{O_2^+,X}}, \tag{17}$$

where $\sigma_{i^+,X}$ represents the cross section for the production of the ion i^+ by interaction of the neutral species α with the energetic particle X. The molecular ions are produced through single nondissociative electron capture and single nondissociative ionization. The atomic ions are a product of single dissociative capture and single dissociative ionization. Multiple ionization, the processes involving H^-, such as the double-electron capture by a proton or the electron capture by H, as well as the processes involving O^- are neglected [*Pilipenko and Fogel'*, 1965; *Browning and Gilbody*, 1968; *McNeal and Clark*, 1969; *McNeal and Birely*, 1973, and references therein; *Rudd et al.*, 1985]. The fragmentation ratios for the couples (N_2,H^+) and (O_2,H^+) are from *Browning and Gilbody* [1968], and that associated with (O_2,H) is from *Pilipenko and Fogel'* [1965]. For (N_2,H) we obtain the fragmentation ratio from the total ionization cross section given by *Basu et al.* [1987] and from the dissociative ionization cross section given by *Kozelov and Ivanov* [1992]. All these fragmentation ratios are parameterized as given in Table 3.

Table 3. Parameterization of the Fragmentation Ratio

	(N_2, H^+)	(N_2, H)	(O_2, H^+)	(O_2, H)
b_0	3.85×10^{-2}	4.56×10^{-2}	8.90×10^{-2}	3.15×10^{-1}
b_1	3.03×10^{-2}	1.27×10^{-2}	3.95×10^{-2}	2.19×10^{-2}
b_2	-4.74×10^{-4}	-1.15×10^{-4}	-4.21×10^{-4}	-3.92×10^{-4}
$E_{0\max}$, keV	15	20	20	15

For $E_0 \le E_{0\max}$, $\mathcal{F}_{\alpha,X}(E_0) = \sum_l b_l\ (2\,E_0)^l$ with E_0 in keV. For $E_{0\max} < E_0 \le 20$ keV, $\mathcal{F}_{\alpha,X}(E_0) = \mathcal{F}_{\alpha,X}(E_{0\max})$.

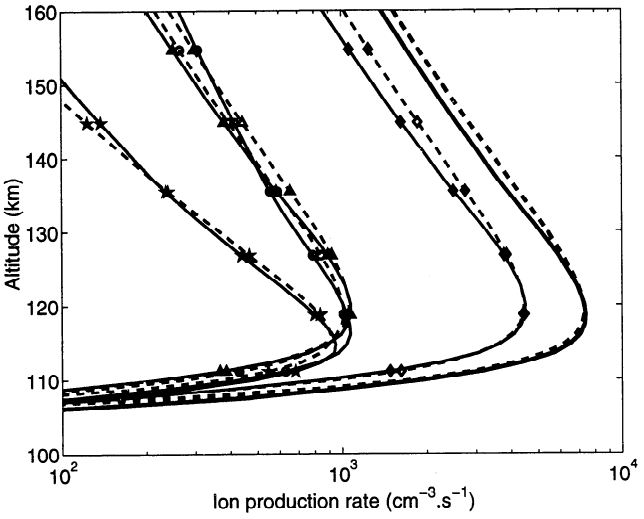

Figure 5. Altitude profiles of the ion production rate for a characteristic energy E_0 of 5 keV and an incident energy flux Q_0 of 1 erg cm^{-2} s^{-1}. The diamonds correspond to N_2^+, the triangles correspond to N^+, the stars correspond to O_2^+, and the circles correspond to O^+. The lines without symbols represent the total of all contributions, i. e., the electron production rate. The solid lines are from the transport code, and the dashed lines are from the parameterization.

The ion production rates can now be computed as follows:

$$
\begin{aligned}
P_{N_2^+} &= \sum_{X=H^+,H} \frac{P_{N_2,X}}{(1+\mathcal{F}_{N_2,X})} \\
P_{N^+} &= \sum_{X=H^+,H} \frac{\mathcal{F}_{N_2,X}\ P_{N_2,X}}{(1+\mathcal{F}_{N_2,X})} \\
P_{O_2^+} &= \sum_{X=H^+,H} \frac{P_{O_2,X}}{(1+\mathcal{F}_{O_2,X})} \\
P_{O^+} &= \sum_{X=H^+,H} \frac{\mathcal{F}_{O_2,X}\ P_{O_2,X}}{(1+\mathcal{F}_{O_2,X})} + P_{O,(H^+ \text{or} H)}.
\end{aligned}
\tag{18}
$$

The parameterized ion production rates are shown with dashed lines in Figure 5 for a characteristic energy E_0 of 5 keV together with the ion production rates from the transport calculation. The fragmentation ratios increase with energy but remain less than 0.5 at $E_0 = 10$ keV. For nitrogen the molecular ion production rates are dominant over the atomic ion production rates, while the total production of the ion O^+ dominates the molecular ion production rate due to the direct contribution from O. Over the whole range of E_0, the difference between the parameterization and the reference ion production rate is less than 20% (at the peak), and the error of the peak altitude is less than ±3 km (except for E_0 lower than 3 keV, for which the difference can be up to 7 km).

3. The 1D-in-Space Thermosphere-Ionosphere Global Mean Model

The effect of ionization by an incident energetic proton beam is included in the 1D-in-space Thermosphere-Ionosphere Global Mean Model [*Roble*, 1995, and references therein]. This model is a self-consistent model representing a latitudinal average of the coupled thermosphere and ionosphere. The continuity equation is solved for O^+ including ambipolar diffusion and then for NO^+, O_2^+, N_2^+, and N^+, assuming photochemical equilibrium with respect to the O^+ density profile. The continuity equation is also solved for the major neutral constituents N_2, O_2, and O as well as for the minor species NO, $N(^2D)$, and $N(^4D)$. The model also solves the electron, ion, and neutral gas thermodynamic equations. The sources of ionization, dissociation, excitation, and heating by solar UV and EUV radiation, electron auroral precipitation, geocorona UV and EUV radiation, and galactic and solar X rays are already included in the Global Mean Model. In addition, we include, for the very first time, the auroral keV proton precipitation: the ion production rates parameterized in section 2 are introduced as source terms in the continuity equations of N_2^+, N^+, O_2^+, and O^+. We use the Global Mean Model to establish background conditions. The proton precipitation is treated as a column model acting on the global mean background. The advantage of the Global Mean Model over an empirical model like MSIS is that it is self-consistent and allows the neutral and ionized atmosphere to respond to the auroral precipitation instead of remaining constant [*Roble*, 1995].

The Global Mean Model is first run with only a solar background associated with a solar $F_{10.7}$ index of 150, until reaching steady state. Starting from this base case, the model is run for 2 hours with constant electron precipitation (case 1) and with constant combined electron and proton precipitation (case 2). The comparison of these two cases allows us to show qualitatively what is missed in neglecting proton precipitation. The time step is chosen as 5 min, and the computation is performed from about 40 km up to about 400 km. The characteristic energy E_0 of the Maxwellian distribution is taken to be 2 keV for the incident electrons and to be 5 keV for the incident protons. The total incident energy flux Q_0 is chosen as 6 ergs cm^{-2} s^{-1} for electrons and 2.5 ergs cm^{-2} s^{-1} for protons. These values are valid for medium conditions of magnetic activity. The density profiles of different atmospheric constituents are shown by solid lines for case 1 and by dashed lines for case 2 in Figures 6a and 6b.

By adding the proton flux, the electron density increases up to 200% and exhibits a second peak around 130 km. The protons deposit their energy at a higher-altitude region compared with electrons although the protons were given a higher characteristic energy. The difference in the altitude profile leads to the increase of

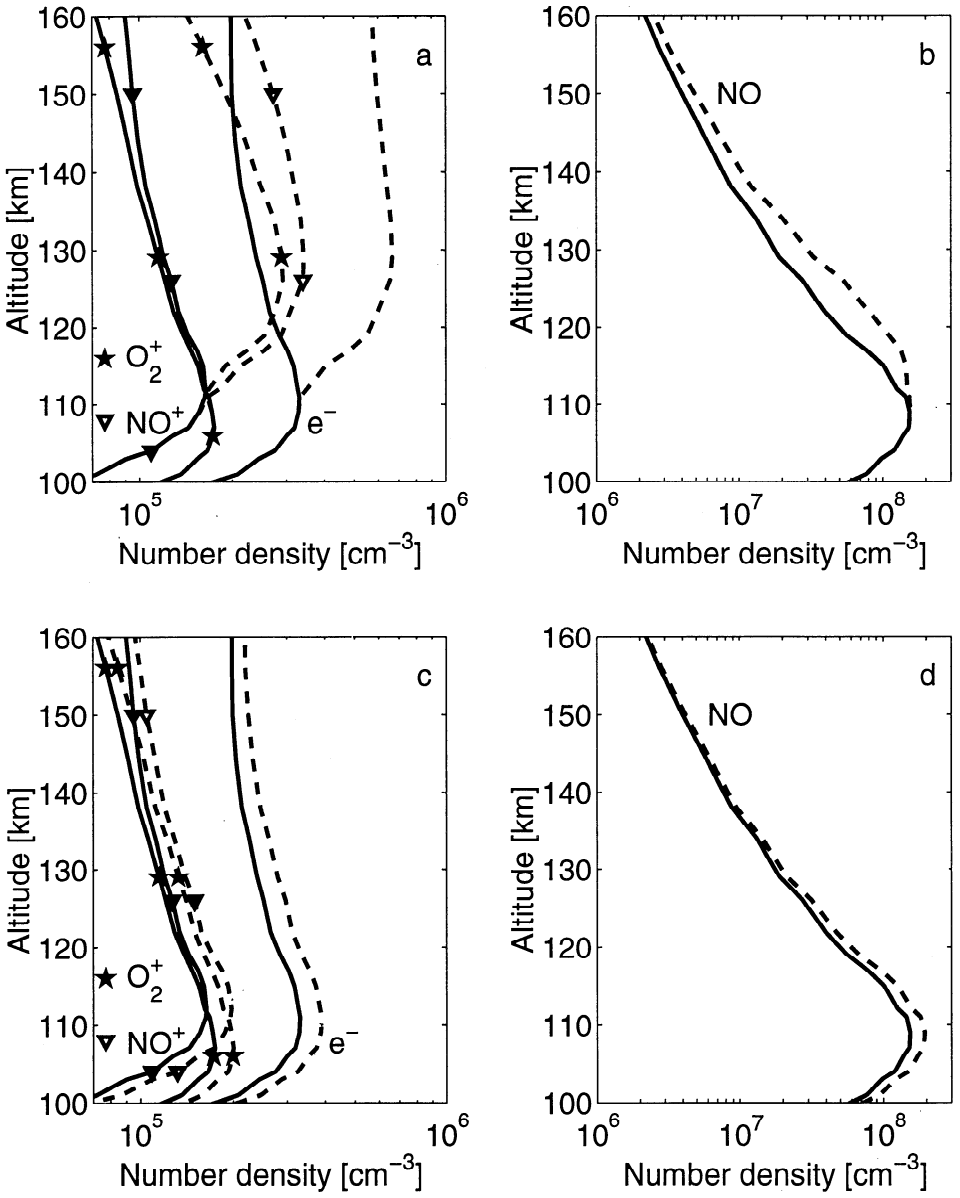

Figure 6. (a, b) Altitude profiles computed with the 1D-in-space Global Mean Model including electron precipitation (case 1, solid lines) or including combined electron-proton precipitation (case 2, dashed lines) of different fields. (c, d) Same as in Figures 6a and 6b except case 3 instead of case 2 (dashed lines) where all particles are assumed to be electrons.

electron density. With the increase in the electron density the conductivities are also affected by the proton precipitation. Including protons leads to an enhancement of 200%, 350%, and 166% for the Pedersen, Hall, and parallel conductivities, respectively. The two major ions of the E region, O_2^+ and NO^+, also show a large density enhancement of 160% and 200%, respectively. The direct production of O_2^+ by the interaction of the proton beam with O_2 is a minor source compared to the reaction $N_2^+ + O_2 \rightarrow O_2^+ + N_2$, and NO^+ is only produced via chemistry: N_2^+, N^+, O_2^+, and O^+, produced directly, react with O, O_2, N, and N_2, respectively, leading to NO^+.

The major neutral species (N_2, O_2, and O) have a density large enough that they are not significantly perturbed by the chemistry resulting from the proton precipitation in the E region. However, minor species like NO are sensitive to this chemistry, as shown in Figure 6b. NO^+ undergoes a dissociative recombination which mainly leads to the production of $N(^2D)$. This reacts with O_2 to produce NO [*Barth*, 1992]. The result is an increase of NO density up to 100% at some altitudes due to the proton precipitation.

The 1D-in-space Global Mean Model exposes the main response of the atmosphere to proton precipitation. To investigate further the role played by protons,

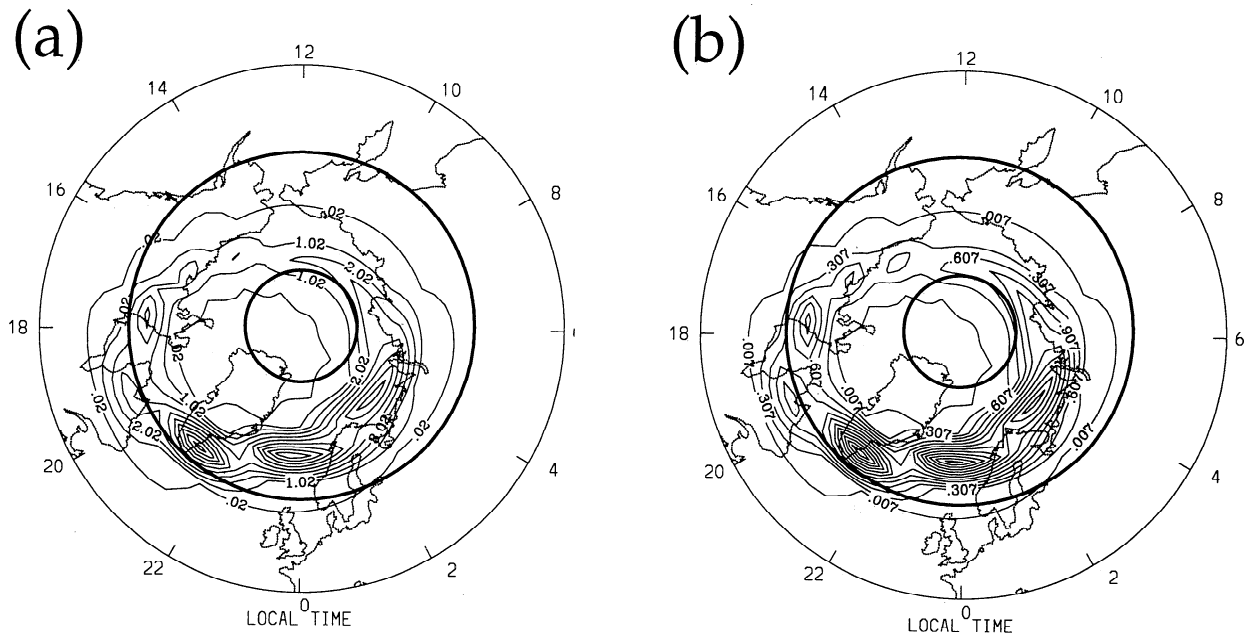

Figure 7. Polar view over the Northern Hemisphere of the energy flux Q_0 for the incident particles: (a) for electrons and (b) for protons. The perimeter in latitude is at 45°. The two thick solid circles represent a latitude of 60° and of 80°. The contours for the energy flux Q_0 are labeled in ergs cm^{-2} s^{-1}. The characteristic energy varies along the oval with the highest values at magnetic midnight.

we studied another case (case 3) where the proton precipitation is simulated by electrons. Electrons penetrate deeper than protons for the same characteristic energy. We constructed case 3 such that the electrons that are meant to simulate the protons have a lower characteristic energy (2 keV) and carry the same energy flux as the protons of case 2. A similar approach has been used in global studies and the incident particle flux defined by satellite data [*Fuller-Rowell and Evans*, 1987; *Fuller-Rowell et al.*, 1996]. The electron density profiles for case 1 and case 3 are presented in Figure 6c. Figure 6d shows the resulting NO profiles. Figures 6c and 6d must be compared to Figures 6a and 6b. The density enhancement from the additional electrons in case 3 is between 20% and 30% over case 1. This is much less compared with the enhancement in case 2, where the additional flux was carried by protons. This comparison shows clearly that protons cannot simply be treated as if they were electrons. If we had chosen to simulate the protons by electrons of the same characteristic energy, the comparison would be even worse. The cross sections and energy losses of protons and electrons are different, and the energy loss per electron produced in a proton beam (see Figure 2) is lower than that of electrons (typically around 35 eV [*Strickland et al.*, 1993]). Protons are more efficient in the production of proto-electrons compared to the secondary electron production in electron aurora.

The 1D-in-space Global Mean Model shows the effect induced by protons on different ionospheric parameters: electron, ion, and neutral densities and conductivities. Electron and proton precipitations have not only different effects on the ionosphere but occur in different locations and with separate characteristic energies and energy fluxes. We will now include the proton precipitation in a global model to investigate the effects on a planetary scale.

4. The 3D-in-Space Thermosphere-Ionosphere Electrodynamics General Circulation Model

The effect of ionization by proton precipitation is examined by using the NCAR TIE-GCM. This model is a three-dimensional, time-dependent model of the Earth's upper atmosphere extending from 95 up to about 800 km [*Roble et al.*, 1988; *Richmond et al.*, 1992]. The continuity, momentum, and thermodynamic equations are solved for the neutral gas and the plasma with a self-consistent aeronomy scheme for the coupled thermosphere and ionosphere system. The state equation of an ideal gas is applied. The model computes self-consistently the coupled thermospheric-ionospheric dynamics, the associated dynamo-electric fields and currents, and the electrodynamic feedback on the neutral and plasma motions and thermodynamics. The vertical resolution is 2 grid points per scale height with a total of 29 points extending between 95 and 800 km. The horizontal resolution is 5° in latitude by 5° in longitude. The temporal resolution is of about 5 min.

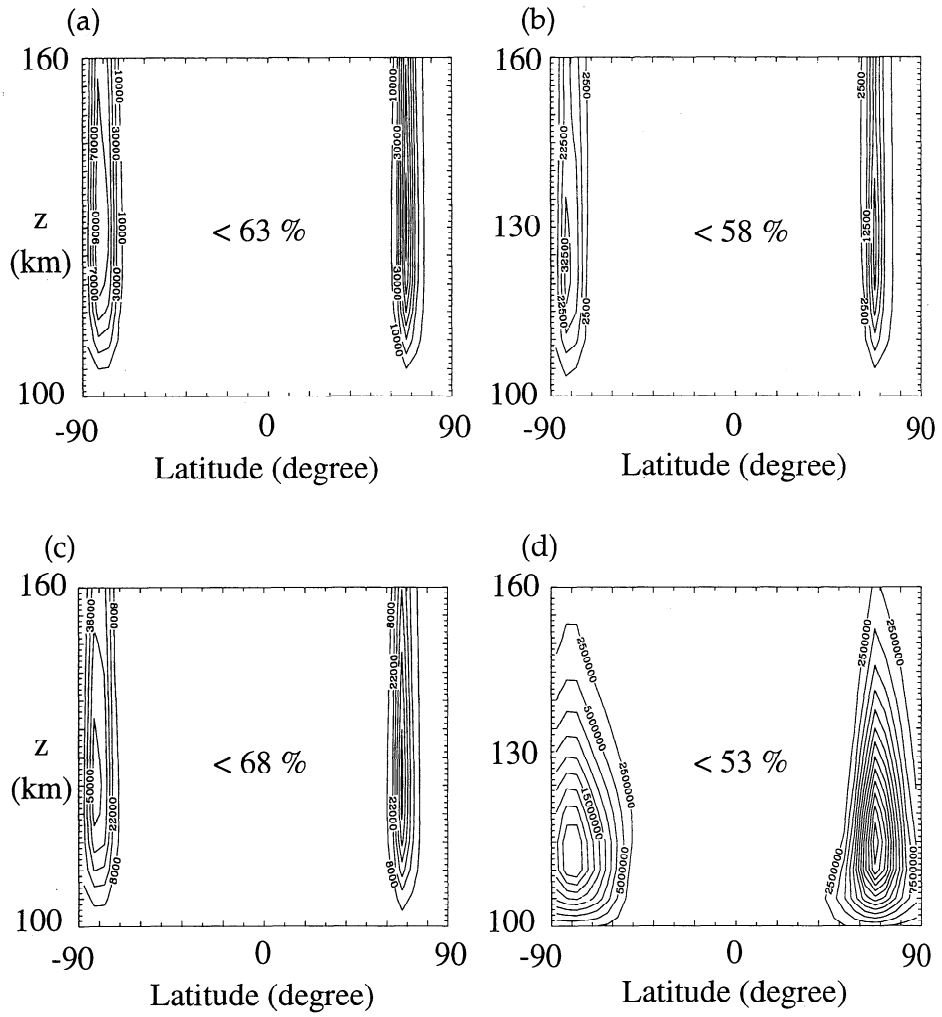

Figure 8. Latitudinal cuts at 0000 Solar Local Time (SLT) as function of latitude and altitude of the density increase, after 24 hours from the start of the simulation for (a) electrons, (b) O_2^+, (c) NO^+, and (d) NO. The density increases are in cm^{-3}. Two successive contour lines are separated by 2×10^4 cm^{-3} for the electron density, by 10^4 cm^{-3} for the O_2^+ density, by 1.4×10^4 cm^{-3} for the NO^+ density, and by 2.5×10^6 cm^{-3} for the NO density. For a given species at a given location the plots show the increase of the density obtained by including proton precipitation (case 5) in addition to the electron precipitation (case 4). The maximum relative increase in percent, in the area of significant absolute difference, is given for each constituent.

The input parameters of the global model are the solar EUV-UV spectral irradiance, the auroral particle fluxes and the electric potential in the polar caps, and, at the lower altitude boundary, the upward propagating atmospheric tides and gravity waves. The model computes the density of the major neutral constituents (N_2, O_2, and O), some minor constituents ($N(^2D)$, $N(^4S)$, NO, He, and Ar), and the density of electrons and key ions (O^+, O_2^+, N_2^+, N^+, and NO^+). The neutral zonal and meridional winds, the ion drift, the electron, ion, and neutral temperatures, as well as the electric potential are also computed, among other fields.

To study the influence of keV protons, the parameterization of the electron and ion production rates from section 2 is included in the continuity equations of O^+, O_2^+, N_2^+, and N^+. Starting from a base case valid for equinox and associated with a solar index $F_{10.7}$ of 150 and very soft electron precipitation, we compare two runs for one simulated day: one including harder electron precipitation (case 4) and the other including both harder electron and proton precipitations (case 5). All plots presented are at 0000 UT corresponding to a time 24 hours into the simulation. The variation of the characteristic energy and of the energy flux in the auroral oval is as defined by *Roble and Ridley* [1987]. The electron and proton precipitations are colocated. Over the auroral oval the characteristic energy E_0 undergoes a Solar Local Time (SLT) variation from 1.5 keV on the dayside to 4.0 keV on the nightside for electrons and from 3.0 keV on the dayside to 10.0 keV on the night-

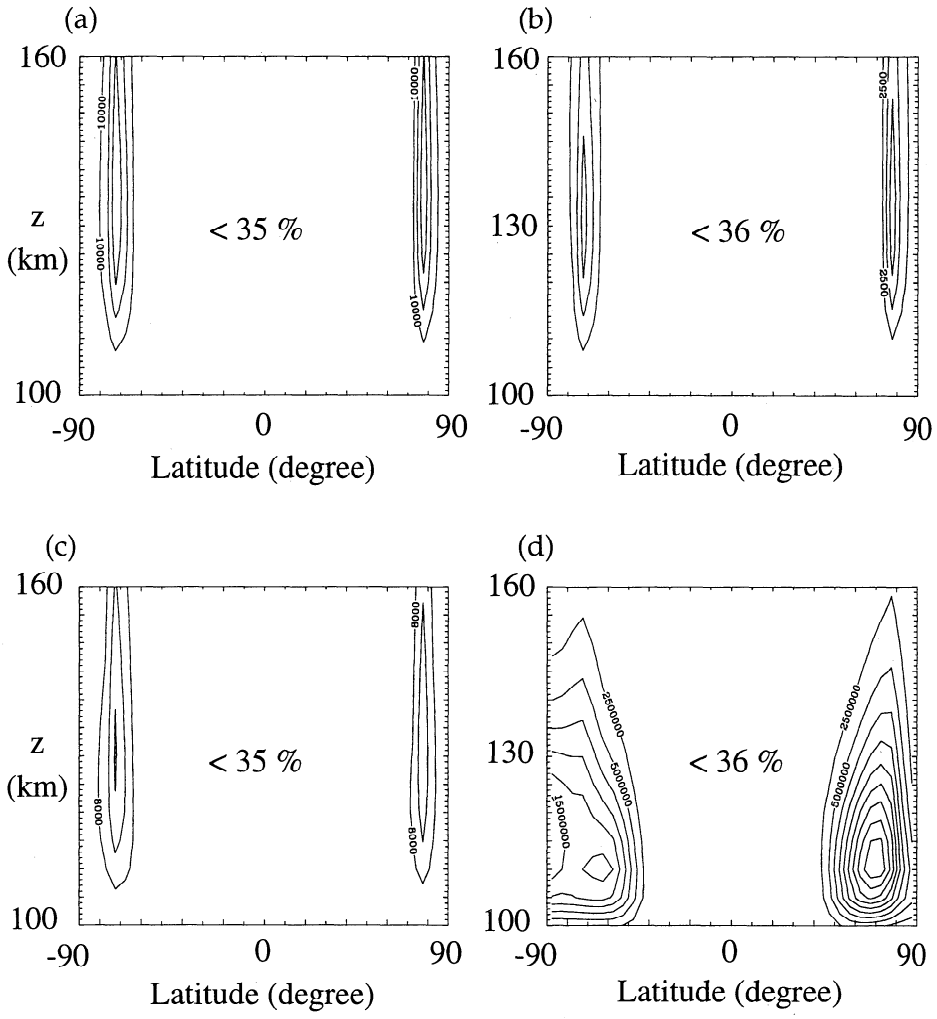

Figure 9. Same as Figure 8, except at 1200 SLT.

side for protons. Along the centerline of the auroral oval the energy flux Q_0 varies from 2.0 ergs cm^{-2} s^{-1} on the dayside to 10.0 ergs cm^{-2} s^{-1} on the nightside for electrons and from 1.0 to 3.5 ergs cm^{-2} s^{-1} for protons (see Figures 7a and 7b). The latitudinal variation of the incident energy flux is assumed to be Gaussian. Note that the individual maxima appearing in the incident energy fluxes are an artifact of the sampling of the auroral oval on the large grid scale of the model in latitude and longitude. The values chosen for E_0 and Q_0 are valid for medium conditions of magnetic activity. The ratio of the energy fluxes between electrons and protons is of the order of that given by the statistical model of *Hardy et al.* [1989] based on satellite measurements. We should note that we have chosen an extreme case, where the proton precipitation is at the upper limit of the observations.

A comparison of case 4 (for which only electron precipitation is included) and case 5 (for which electron and proton precipitations are included) at 0000 SLT is shown in Figure 8 for the electron density, O_2^+ density, NO^+ density, and NO density. For a given species and a given location, Figures 8a–8d show the increase of the density obtained by including proton precipitation (case 5) in addition to the electron precipitation (case 4). We have plotted the absolute difference of the density as a function of latitude and altitude. The absolute difference is more relevant for the study of spatial features than the relative difference is. The maximum relative increase in percent, in the area of significant absolute difference, is given for each constituent. The density increases up to 63, 58, and 68% for electrons, O_2^+, and NO^+, respectively (refer to Figures 8a–8c). The ion densities are affected only inside the precipitation region. The increase of the NO density from the proton precipitation is up to 53% in the E region but affects a larger area outside the precipitation region. The peak of the density difference is near the altitude of the NO density maximum, around 110 km.

Figure 9 shows the same plots of density increases induced in including proton precipitation, except for 1200 SLT. The enhancement in density is up to 35, 36, 35, and 36% for electrons, O_2^+, NO^+, and neutral NO, respectively. Because of the lower incident proton energy flux on the dayside, these increases are much less compared with those on the nightside (Figure 8). The alti-

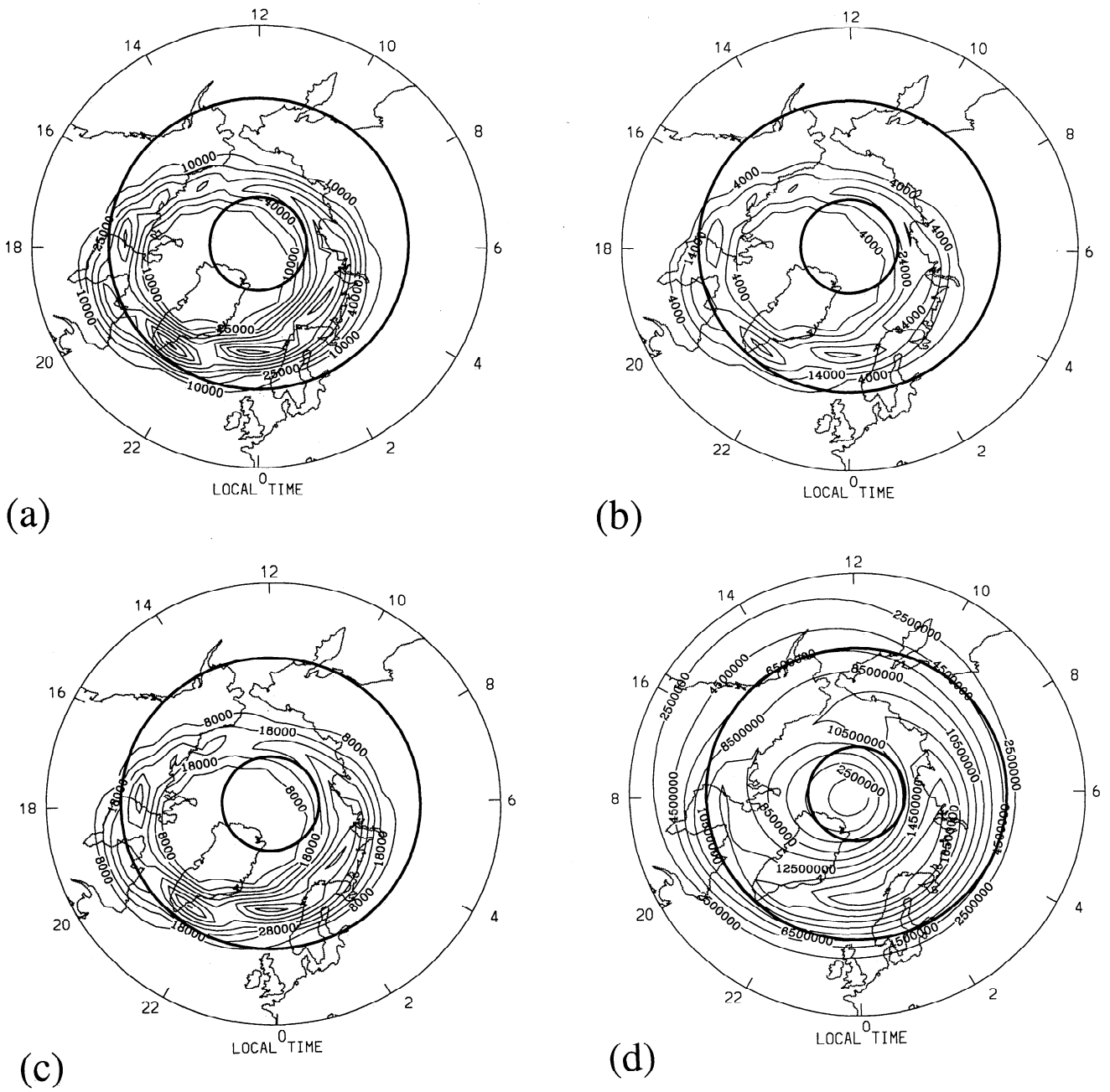

Figure 10. Same as Figures 8 and 9 but presented as a horizontal slice through the Thermosphere-Ionosphere Electrodynamics General Circulation Model (TIE-GCM) at 130 km altitude, showing the density increase due to proton precipitation after 24 hours from the start of the simulation for (a) electrons, (b) O_2^+, (c) NO^+, and (d) NO. Note that the short-lived ion density increases only in the region of precipitation (see Figure 7b), while the NO density increase affects a much larger area. The perimeter in latitude is at 45° and the two thick solid circles represent a latitude of 60° and 80°.

tude of the maximum difference in density is higher on the dayside case compared with that on the nightside case, because of the lower characteristic proton energy on the dayside. In addition, the increase of neutral temperature from solar heating causes an expansion of the atmosphere, which also affects the penetration of energetic particles.

Figure 10 shows a polar view of the density increase due to proton precipitation of electrons, O_2^+, NO^+, and NO at 130 km altitude. It appears clearly that the electron and NO^+ densities increase in the regions where there is local ionization by the proton precipitation, that is, inside the auroral oval (shown in Figure 7b). The maxima in density increase are located exactly where an enhancement of the proton energy flux is. The lifetime of the electrons and ions at this altitude is short enough that there is no change outside the auroral oval.

On the other hand, the increase in NO density is

smoother and spread out in latitude. The long lifetime of NO on the nightside, the rotation of the Earth, and thermospheric convection combine to spread the NO. Inside the auroral oval in the morning sector, high values of the NO density are a remnant of earlier precipitation. Thermospheric convection carries NO from the auroral zone to lower latitudes. Once the NO moves into the dayside, dissociation by solar EUV removes the NO. Although the effect of proton precipitation on the temperature and the dynamic structure of the E region is small, it appears clearly that there are significant effects on the compositional structure of the ionosphere and of the minor neutral constituents.

5. Discussion and Summary

In order to investigate the impact of proton precipitation in the auroral E region on both the thermosphere and the ionosphere on a planetary scale, we have developed simplified relations for the electron and ion production rates induced by incident protons. The incident proton flux at the top of the atmosphere is assumed to be isotropic over the downward hemisphere, with a Maxwellian distribution in energy. The parameterization is limited to characteristic energies in the $1-20$ keV range. The spreading of the beam, the magnetic mirror, and the collisional angular redistribution are neglected.

The derivation of the parameterized electron and ion production rates is explicitly given such that this parameterization can be included in large-scale ionospheric models. This derivation assumes that the electron and ion production rates are proportional to the energy deposition rate and that the mean loss function is approximated by a power law. The parameterized ion production rates for individual species are given by (18) where the parameters are given by Table 3 and (15). The energy loss in (15) is given in Table 2, while the energy deposition rate can be obtained from (2) in combination with (10) and (11) and Table 1. The development as well as the validation of this parameterization have been performed by comparing with a full proton transport code. The uncertainties due to the parameterization are less than 10% of the electron production rate and less than 20% of the ion production rates at the altitude of the peak.

By including these parameterized electron and ion production rates in the 1D-in-space Thermosphere-Ionosphere Global Mean Model, we have shown that in the E region, protons can have a significant impact on the densities of electrons, major ions (O_2^+ and NO^+), and minor constituents. As a result of the enhancement in the electron density, the conductivities are also affected. We have also shown that simulating the proton energy flux by including it with the precipitating electrons causes significant underestimation of the ionospheric response: energetic protons spend their energy in a different altitude range as comparable energetic electrons and are more efficient in producing secondary electrons. It is therefore important to consider protons separately as a source of ionization.

To investigate the effect of proton precipitation on a planetary scale, the parameterized electron and ion production rates have been included in the global three-dimensional (3-D) NCAR TIE-GCM. While the winds and temperatures are not significantly changed by including proton precipitation, the influence on the ionospheric and thermospheric composition is significant in the E region. The electron, O_2^+, NO^+, and neutral NO densities are enhanced up to 60%. The increase on the nightside is higher than that on the dayside as the energy flux of the incident protons is typically larger on the nightside.

The incident protons are assumed to have a Maxwellian distribution in energy. This distribution is often used in proton transport studies [e.g., *Strickland et al.*, 1993; *Galand et al.*, 1997] and has been observed in the 30 eV–30 keV range but is not always appropriate [*Hardy et al.*, 1989]. Observations at higher energies have shown that the proton flux has a high-energy tail above that of a Maxwellian. This high-energy tail can be modeled by a Maxwellian with higher characteristic energies [*Codrescu et al.*, 1997] or by a power law (using a kappa distribution over the 100 eV–100 keV range) [*Decker et al.*, 1996]. Such an additional energetic population above typically 30 keV would further increase the impact of protons on the atmosphere, especially at lower altitudes. To include the source of ionization and production of electrons of such energetic protons requires further studies. The present parameterization is not intended to include the whole high-energy proton population with energies above 30 keV.

The present study clearly demonstrates that the proton component of particle precipitation must be considered in global ionosphere-thermosphere models. Although the values taken for the incident electron and proton fluxes for the planetary-scale study are in a realistic range (even though at the upper limit), the spatial structure of the energy flux in the auroral oval has been very much simplified: the electron and proton ovals are assumed symmetric and located at the same position. Observations have shown that the proton oval is shifted from the electron oval equatorward before midnight and polarward after midnight [*Hardy et al.*, 1989]. Realistic electron and proton ovals are asymmetric owing to the westward curvature drift for protons and the eastward drift for electrons [*Codrescu et al.*, 1997]. To account for these spatial distributions in global thermospheric models, statistical patterns derived from satellite observations [*Hardy et al.*, 1989, 1991; *Brautigam et al.*, 1991; *Codrescu et al.*, 1997] are needed.

In the present paper we have focused on the E region. The major effect of protons in this altitude region is the electron and ion production which causes a variation in the atmospheric composition. We plan to extend this study to higher altitudes, which requires the treatment of heating from the proto-electrons. The electrons pro-

duced by keV protons are not energetic enough to cause significant secondary ionization, but they heat the ambient thermal electrons. In the F region the heating from proto-electrons is expected to affect the electron temperature.

Acknowledgments. The authors greatly appreciate assistance from Barbara Emery in obtaining TIE-GCM results. M.G. gratefully acknowledges the financial support of the Advanced Study Program and the High Altitude Observatory, divisions of the National Center for Atmospheric Research (NCAR). M.G. thanks SEC/NOAA for supporting her during the writing of the article. DL was supported by NASA grant NAG5-7683 to the University of Alaska.

Janet G. Luhmann thanks Robert E. Daniell and James R. Sharber for their assistance in evaluating this paper.

References

Anderson, P. C., I. W. McCrea, D. J. Strickland, J. B. Blake, and M. D. Looper, Coordinated EISCAT/DMSP measurements of electron density and energetic electron precipitation, *J. Geophys. Res.*, *102*, 7421-7430, 1997.

Barth, C. A., Nitric oxide in the lower thermosphere, *Planet. Space Sci.*, *40*, 315-336, 1992.

Basu, B., J. R. Jasperse, R. M. Robinson, R. R. Vondrak, and D. S. Evans, Linear transport theory of auroral proton precipitation: A comparison with observations, *J. Geophys. Res.*, *92*, 5920-5932, 1987.

Basu, B., J. R. Jasperse, D. J. Strickland, and R. E. Daniell, Transport-theoretic model for the electron-proton-hydrogen atom aurora, 1, Theory, *J. Geophys. Res.*, *98*, 21,517-21,532, 1993.

Brautigam, D. H., M. S. Gussenhoven, and D. A. Hardy, A statistical study on the effects of IMF Bz and solar wind speed on auroral ion and electron precipitation, *J. Geophys. Res.*, *96*, 5525-5538, 1991.

Browning, R., and H. B. Gilbody, Fragmentation of molecular gases by 5-45 keV protons, *J. Phys. B At. Mol. Phys.*, *1*, 1149-1156, 1968.

Codrescu, M. V., T. J. Fuller-Rowell, R. G. Roble, and D. S. Evans, Medium energy particle precipitation influences on the mesosphere and lower thermosphere, *J. Geophys. Res.*, *102*, 19,977-19,987, 1997.

Decker, D. T., B. V. Kozelov, B. Basu, J. R. Jasperse, and V. E. Ivanov, Collisional degradation of the proton-H atom fluxes in the atmosphere: A comparison of theoretical techniques, *J. Geophys. Res.*, *101*, 26,947-26,960, 1996.

Fuller-Rowell, T. J., and D. S. Evans, Height-integrated Pedersen and Hall conductivity patterns inferred from the TIROS-NOAA satellite data, *J. Geophys. Res.*, *92*, 7606-7618, 1987.

Fuller-Rowell, T. J., M. V. Codrescu, H. Rishbeth, R. J. Moffett, and S. Quegan, On the seasonal response of the thermosphere and ionosphere to geomagnetic storms, *J. Geophys. Res.*, *101*, 2343-2353, 1996.

Galand, M., Transport des protons dans l'ionosphère aurorale, Ph.D. thesis, Univ. Grenoble I, Grenoble, France, 1996.

Galand, M., and A. D. Richmond, Magnetic mirroring in an incident proton beam, *J. Geophys. Res.*, *104*, 4447-4455, 1999.

Galand, M., J. Lilensten, W. Kofman, and R. B. Sidje, Proton transport model in the ionosphere, 1, Multistream approach of the transport equations, *J. Geophys. Res.*, *102*, 22,261-22,272, 1997.

Galand, M., J. Lilensten, W. Kofman, and D. Lummerzheim, Proton transport model in the ionosphere, 2, Influence of magnetic mirroring and collisions on the angular redistribution in a proton beam, *Ann. Geophys.*, *16*, 1308-1321, 1998.

Hardy, D. A., M. S. Gussenhoven, and D. Brautigam, A statistical model of auroral ion precipitation, *J. Geophys. Res.*, *94*, 370-392, 1989.

Hardy, D. A., W. McNeil, M. S. Gussenhoven, and D. Brautigam, A statistical model of auroral ion precipitation, 2, Functional representation of the average patterns, *J. Geophys. Res.*, *96*, 5539-5547, 1991.

Hedin, A. E., Extension of the MSIS thermosphere model into the middle and lower atmosphere, *J. Geophys. Res.*, *96*, 1159-1172, 1991.

Jackman, C. H., J. E. Frederick, and R. S. Stolarski, Production of odd nitrogen in the stratosphere and mesosphere: An intercomparison of source strengths, *J. Geophys. Res.*, *85*, 7495-7505, 1980.

Jasperse, J. R., and B. Basu, Transport theoretic solutions for auroral proton and H atom fluxes and related quantities, *J. Geophys. Res.*, *87*, 811-822, 1982.

Kozelov, B. V., Influence of the dipolar magnetic field on transport of proton-H atom fluxes in the atmosphere, *Ann. Geophys.*, *11*, 697-704, 1993.

Kozelov, B. V., and V. E. Ivanov, Monte Carlo calculation of proton-hydrogen atom transport in N_2, *Planet. Space Sci.*, *40*, 1503-1511, 1992.

Kozelov, B. V., and V. E. Ivanov, Effective energy loss per electron-ion pair in proton aurora, *Ann. Geophys.*, *12*, 1071-1075, 1994.

Lilensten, J., and M. Galand, Proton-electron precipitation effects on the electron production and density above EISCAT (Tromsø) and ESR, *Ann. Geophys.*, *16*, 1299-1307, 1998.

Lummerzheim, D., Comparison of energy dissipation functions for high energy auroral electron and ion precipitation, *Geophys. Inst. Rep.*, *UAG-R-318*, pp. 1-25, Univ. of Alaska, Fairbanks, 1992.

McNeal, R. J., and J. H. Birely, Laboratory studies of collisions of energetic H^+ and hydrogen with atmospheric constituents, *Rev. Geophys*, *11*, 633-693, 1973.

McNeal, R. J., and D. C. Clark, Ionization and excitation of nitrogen by protons and hydrogen atoms in the energy range 1-25 keV, *J. Geophys. Res.*, *74*, 5065-5072, 1969.

Newell, P. T., W. J. Burke, C.-I. Meng, E. R. Sanchez, and M. E. Greenspan, Identification and observations of the plasma mantle at low altitude, *J. Geophys. Res.*, *96*, 35-45, 1991.

Pilipenko, D. V., and Y. M. Fogel', Composition of slow ions formed on passage of fast hydrogen atoms through molecular gases, *Sov. Phys. JETP* Engl. Transl., *15*, 266-273, 1965.

Rees, M. H., Auroral ionization and excitation by incident energetic electrons, *Planet. Space Sci.*, *11*, 1209-1218, 1963.

Rees, M. H., On the interaction of auroral protons with the Earth's atmosphere, *Planet. Space Sci.*, *30*, 463-472, 1982.

Rees, M. H., Modeling of the heating and ionizing of the polar thermosphere by magnetospheric electron and ion precipitation, *Phys. Scr.*, *T 18*, 249-255, 1987.

Rees, M. H., *Physics and Chemistry of the Upper Atmosphere*, *Cambridge Atmos. Space Sci. Ser.*, Cambridge Univ. Press, New York, 1989.

Reid, G. C., A study of the enhanced ionization produced by solar protons during a polar cap absorption event, *J. Geophys. Res.*, *66*, 4071-4085, 1961.

Richmond, A. D., E. C. Ridley, and R. G. Roble, A thermosphere/ionosphere general circulation model with coupled electrodynamics, *Geophys. Res. Lett.*, *19*, 601-604, 1992.

Roble, R. G., The polar lower thermosphere, *Planet. Space Sci.*, *40*, 271-297, 1992.

Roble, R. G., Energetics of the mesosphere and thermosphere, in *The Upper Mesosphere and Lower Thermosphere: A Review of Experiment and Theory, Geophys. Monogr. Ser.*, Vol. 87, edited by R. M. Johnson and T. L. Killeen, pp.1-21, AGU, Washington, D.C., 1995.

Roble, R. G., The NCAR Thermosphere-Ionosphere-Mesosphere-Electrodynamics General Circulation Model (TIME-GCM), in *Solar-Terrestrial Energy Program: Handbook of Ionospheric Models*, edited by R. W. Schunk, pp.281-288, STEP, Logan, UT, 1996.

Roble, R. G., and E. C. Ridley, An auroral model for the NCAR thermospheric general circulation model (TGCM), *Ann. Geophys.*, *6*, 369-382, 1987.

Roble, R. G., E. C. Ridley, A. D. Richmond, and D. E. Dickinson, A coupled Thermosphere/Ionosphere General Circulation Model, *Geophys. Res. Let.*, *15*, 1325-1328, 1988.

Rudd, M. E., Y.-K. Kim, D. H. Madison, and J. W. Gallagher, Electron production in proton collisions: Total cross sections, *Rev. Mod. Phys.*, *57*, 965-993, 1985.

Senior, C., J. R. Sharber, O. de la Beaujardière, R. A. Heelis, D. S. Evans, J. D. Winningham, M. Sugiura, and W. R. Hoegy, *E* and *F* region study of the evening sector auroral oval: A Chatanika/Dynamics Explorer 2/NOAA 6 comparison, *J. Geophys. Res.*, *92*, 2477-2494, 1987.

Solomon, S. C., C. A. Barth, and S. M. Bailey, Auroral production of nitric oxide measured by the SNOE satellite, *Geophys. Res. Lett.*, *26*, 1259-1262, 1999.

Søraas, F., H. R. Lindalen, K. Måseide, A. Egeland, T. A. Sten, and D. S. Evans, Proton precipitation and the H_β emission in a postbreakup auroral glow, *J. Geophys. Res.*, *79*, 1851-1859, 1974.

Strickland, D. J., R. E. Daniell Jr., J. R. Jasperse, and B. Basu, Transport-theoretic model for the electron-proton-hydrogen atom aurora, 2, Model results, *J. Geophys. Res.*, *98*, 21,533-21,548, 1993.

M. Galand, Space Environment Center, National Oceanic and Atmospheric Administration, 325 Broadway, Boulder, CO 80303. (mgaland@sec.noaa.gov)

D. Lummerzheim, Geophysical Institute, University of Alaska, 903 Koyukuk Drive, Fairbanks, AK 99775.

R. G. Roble, High Altitude Observatory, National Center for Atmospheric Research, 3450 Mitchell Lane, Boulder, CO 80301.

(Received June 8, 1999; revised July 30, 1999;
accepted August 18, 1999.)